IEEE Photonics Journal
An IEEE Photonics Society Publication

Multitone Photoconductive Sensors for Free-Space Optics

Volume 2, Number 4, August 2010

X. Jin, Student Member, IEEE
J. F. Holzman, Member, IEEE

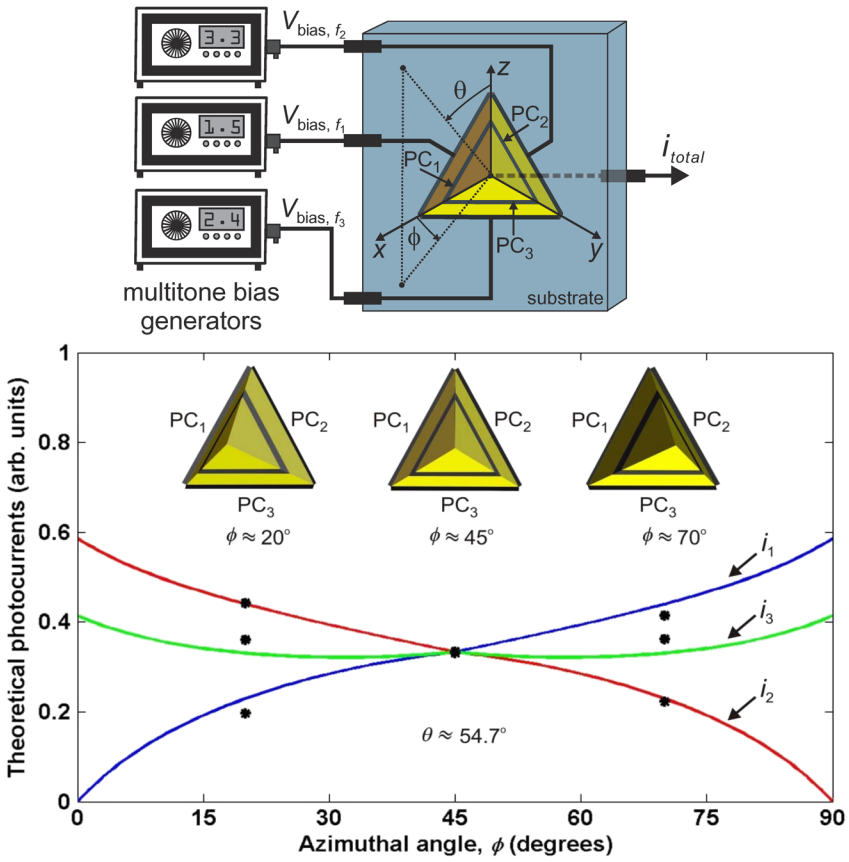

DOI: 10.1109/JPHOT.2010.2057413
1943-0655/$26.00 ©2010 IEEE

IEEE photonics SOCIETY

IEEE

Multitone Photoconductive Sensors for Free-Space Optics

X. Jin, *Student Member, IEEE*, and J. F. Holzman, *Member, IEEE*

Integrated Optics Laboratory, School of Engineering, University of British Columbia–Okanagan, Kelowna, BC V1V 1V7, Canada

DOI: 10.1109/JPHOT.2010.2057413
1943-0655/$26.00 ©2010 IEEE

Manuscript received May 28, 2010; revised June 30, 2010; accepted July 2, 2010. Date of publication July 5, 2010; date of current version July 23, 2010. Corresponding author: J. F. Holzman (e-mail: jonathan.holzman@ubc.ca).

Abstract: A multitone frequency-biasing technique is applied to an integrated photoconductive (PC) sensor for application to free-space optical (FSO) communication systems. The introduced technique and integrated device provide the required optical transmission, detection, and retroreflection capabilities for both passive uplink and active downlink operations. The physical structure incorporates three triangular PC switches, with 450-μm GaAs gaps, assembled in a corner-cube retroreflector architecture. The retroreflective nature of the element establishes a bidirectional passive uplink between the PC sensor and transmitter/source, whereas the three PC switches together provide unidirectional reception of incident optical signals during active downlink operation. At the same time, the threefold symmetry of the structure, together with the multitone biasing, provides a frequency-domain balancing mechanism to optimize the sensor alignment. The prototype is presented with both theoretical and experimental analyses, and proof-of-concept FSO communication is demonstrated over an indoor 5-m link length.

Index Terms: Multitone triangulation, optical communication, photoconductive (PC) switching, retroreflection.

1. Introduction

Photodiodes and photoconductive (PC) switches are integral elements in modern optical communications. These light-activated devices can convert incident optical power into electrical photocurrents with high responsivities [1] and response times down to the picosecond level [2]. The physical layouts of standard photodiodes and PC switches are particularly well suited to butt-coupled [3] optical fiber configurations, as the optical power within a fiber can be efficiently coupled to the sensor active region with directionality and alignment at the interface being largely irrelevant. In contrast to this, directionality requirements become particularly important when optical detectors are deployed for multidirectional applications in free-space optical (FSO) communication environments [4]–[6]. Such FSO systems must provide effective optical sensing over a wide range of incident angles. These FSO directionality challenges are addressed in this work.

FSO communication links relay optically encoded information between transmitters (lasers or LEDs) and receivers (photodetectors) in both passive (bidirectional) uplink or active (unidirectional) downlink formats [7]. Passive uplink formats are bidirectional in nature, as their optical transmitters broadcast beams and sample the returning optical signals—which have undergone retroreflection and modulation at the remote receivers. This form of retrocommunication requires both beam modulation and retroreflection at each receiver to encode information onto the beam before its return back to the source. Such systems have the advantage that the receiver sensors can be made

to be largely independent of the directionality through the use of a retroreflector. In contrast with this, active (unidirectional) downlink formats are simpler in form, as these communication systems provide optical signal transmission directly from the laser [8] or LED [9] transmitter to the photodetector on the remote receiver.

An effective FSO receiver should be capable of passive uplink operation, to return information back to the transmitter, and active downlink operation, to record the incident optical signals from the transmitter. Such a receiver should incorporate three fundamental structures: detectors (photodiodes [10] or PC switches [11]), retroreflectors (retrospheres [12] or corner cubes [13]), and modulators (mirror/beam deflectors [7], liquid crystal shutters [14], or multiquantum-well absorbers [15], [16]). When implemented together, these receiver elements can retroreflect modulated incident light back to its source for passive uplink operation and sample the incident light for active downlink operation. Recent research efforts have focused on improvements for these systems in terms of operational bandwidth [17] and small-scale packaging through, for example, Smart Dust technologies [18], [19].

In this paper, a new PC sensor is introduced for operation as an FSO receiver. The PC sensor merges the aforementioned three receiver structures together into one integrated package. In doing this, the structure meets our established two fundamental requirements for simultaneous uplink/downlink operation: i) passive (bidirectional) optical uplink establishment between the PC sensor/receiver and optical source/transmitter and ii) active (unidirectional) optical downlink detection of signals from the source/transmitter to the PC sensor/receiver. At the same time, it is shown that this new device provides an alignment-balancing mechanism to optimize the retroreflection and detection alignment during the above two operational formats.

The first requirement for simultaneous uplink/downlink operation—being based on passive (bidirectional) optical uplink establishment—is met by the retroreflective nature of the presented structure. The PC sensor is assembled in a corner-cube retroreflector geometry, with three orthogonal and reflective Au-coated electrodes. This structure effectively redirects incident light beams back to their respective remote transmitter/source nodes over a broad ($\pi/2$ Steradians) solid angle. At the same time, the returned signals are optically encoded using a Pi-cell LC modulator [20] for their return to the optical source/transmitter in passive uplink operation.

The second requirement for simultaneous uplink/downlink operation—being based on active (unidirectional) downlink detection—is met through the use of multitone, i.e., multifrequency, biasing on the incorporated three integrated and mutually orthogonal PC switches. The three PC sensors together provide downlink optical signal detection at this sensor node when the constituent photocurrents are simultaneously summed through a broadband electronic filter. The spectral width of the electronic filter is sufficiently broad to pass the three bias frequencies and record the *total* incident optical power on the PC gaps. At the same time, the three PC gaps, with their threefold physical symmetry and three distinct bias frequencies, are used independently to triangulate the directionality between this PC sensor node and the remote transmitter/source node. The three bias frequency signals are extracted from the PC sensor output with three narrow-band filters, and differential combinations of the peak amplitudes are used to triangulate and optimize the link alignment by balancing the amplitudes. This optical triangulation method ultimately makes use of the PC sensor photocurrent output and its orientational-dependent weighting of the intensity on each of the three PC switches. The PC switch with the greatest level of illumination will, for example, have the highest peak frequency amplitude, while the PC switch with the lowest level of illumination will have the lowest peak frequency amplitude.

The directionality of this multitone PC sensor is analyzed theoretically and experimentally in this work for both uplink and downlink FSO communication. The physical layout of the PC sensor is introduced in Section 2. Theoretical and experimental responses are then presented in Sections 3 and 4, respectively, and concluding remarks are given in Section 5.

2. Device

The present investigation extends the capabilities of traditional PC switching to multidirectional FSO applications. The added directionality needed for FSO operation in 3-D space is met through the

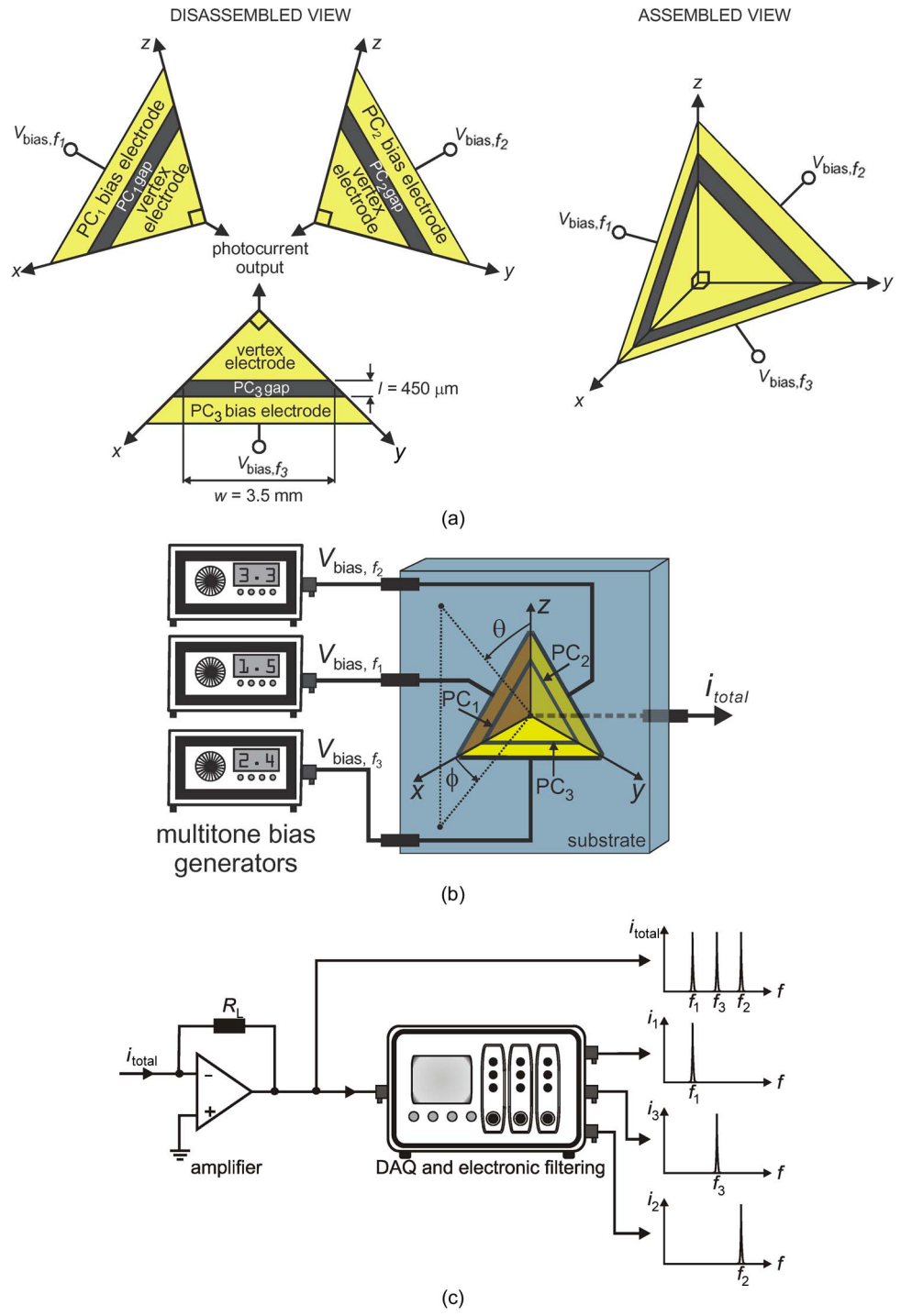

Fig. 1. Schematics are shown for the PC sensor's (a) structure, (b) biasing arrangement, and (c) electronic processing system. The PC structure in (a) consists of three mutually orthogonal PC switches that are biased, as shown in (b), with three distinct frequencies. The resulting output photocurrents are then amplified and electronically filtered with the system shown in (c).

use of multiple PC switches. The three employed PC switches are displayed in the disassembled and assembled views of Fig. 1(a).

The disassembled view of Fig. 1(a) shows three independent PC switches with PC_1 in the x–z plane, PC_2 in the y–z plane, and PC_3 in the x–y plane. Each PC switch is comprised of two separate

metal electrodes of thermally evaporated 150-nm-thick Au layers with 50-nm-thick Cr adhesion layers. Between the electrodes lies the exposed semiconductor PC gap. The photocurrent flows along the PC gap length $l = 450$ μm and across the PC gap width $w = 3.5$ mm. A small PC gap length and large PC gap width are selected here to increase the absolute photocurrent signal levels. At the same time, semi-insulating GaAs is chosen for the PC gap semiconductor material because of its wide direct bandgap (1.43 eV), high resistivity $(10^7\ \Omega \cdot \text{cm})$, high dark resistance $(> 40\ \text{M}\Omega)$, and enhanced electron mobility (8500 $\text{cm}^2\text{V}^{-1}\text{s}^{-1}$). This leads to an appreciable contrast ratio between the relative light and dark PC gap resistance states. Sufficiently large bias voltages are applied to the three bias electrodes at three distinct frequencies, and the light-induced photocurrent components at each of the three bias electrode frequencies are summed on the central vertex electrode in a subsequent electronic processing stage.

To assemble the complete device, each PC switch is diced into right-triangle elements with 5-mm side lengths then optically bonded with Norland Optical Adhesive (NOA 68). The adhesive is cured under an ultraviolet light during a retroreflection-monitoring process. The retroreflected test beam is monitored over a 5-m range, and the PC sensor is adjusted as needed, during this curing process. The assembled structure is shown in Fig. 1(a). The resulting PC sensor has three electrically isolated input bias electrodes—the displayed PC_1, PC_2, and PC_3 bias electrodes—and one continuous and electrically connected vertex electrode for the summed photocurrent signal output. The electrical biasing arrangement is shown in Fig. 1(b). Transmission lines on the surface of the mounting substrate are used to provide electrical access to the three input bias electrodes, and an electrical via hole is used to extract the output signal from the recessed vertex electrode through the back of the mounting substrate.

Incident light on the structure activates the PC_1, PC_2, and PC_3 switches, with the resulting three photocurrent components (at their respective three bias frequencies) appearing on the vertex electrode as the total photocurrent i_{total}. The PC switch seeing the highest intensity will have the lowest gap resistance and highest photocurrent peak frequency. The PC switch seeing the lowest illumination intensity will have the highest gap resistance and lowest photocurrent peak frequency. An amplifier, digital data-acquisition (DAQ) system, and electronic filter are then used to extract the broadband frequency signal i_{total} (as a measure of the total incident optical power during active downlink detection) as well as the isolated narrowband signals i_1, i_2, and i_3 (as measures of the respective PC_1, PC_2, and PC_3 photocurrents during the device triangulation/alignment). The postdetection amplification, digital DAQ, and filtering stages for this processing are shown in Fig. 1(c).

3. Theoretical Analysis

Theoretical responses and design constraints of the PC sensor are introduced in this section. The results are presented in terms of our two defined requirements for FSO sensor operation: passive (bidirectional) optical uplink establishment and active (unidirectional) optical downlink detection.

3.1. Requirement I: Passive (Bidirectional) Optical Uplink Establishment

The bidirectionality of FSO passive optical uplink operation, being based upon optical retroreflection, can be met by the assembled corner-cube structure as it effectively redirects incident light back to its transmitter/source. Incoming light rays with normalized directional cosine components of n_1, n_2, and n_3 in the x-, y-, and z-directions, respectively, can undergo three internal reflections within the corner cube and have each of these directional cosine components flipped by the respective electrode mirrors in the x–z plane, y–z plane, and x–y plane.

The required retroreflection is carried out by the surfaces of the central vertex electrode, the three bias electrodes, and (to a lesser extent) the three PC gaps. Au metallization, with its large reflectivity $R = 97\%$, is used for the electrodes to maximize the retroreflected power and minimize the angular dependence of the reflections. Moreover, the retroreflection contributions from the PC gaps—being less reflective than their surrounding Au surfaces—are minimized through the use of a sufficiently

small PC gap area ($lw \ll 12.5$ mm^2). This ensures that the effective retroreflection area of the device is dominated by the highly reflective Au electrode surfaces.

For the final step in establishing the passive optical uplink, the retroreflecting structure is made capable of optical modulation. This is accomplished through the use of a high-speed Pi-cell LC modulator. The modulator is mounted over the triangular entrance interface of the PC sensor. An external electrical signal is used to provide optical loss modulation in the shutter and encode information onto the incident/retroreflected beams for their eventual return to their respective remote transmitter/source node(s).

The retroreflection efficiency of the structure, being defined as the retroreflected power from the device versus the incident power on the device, will be a function of the incident light ray orientations within the sensor. The orientation for optimal retroreflection efficiency can be found by a straightforward ray-based analysis of the PC sensor. A Matlab model is used to accomplish this by illuminating the device with a sufficiently dense array of incident optical rays and recording the number of successfully retroreflected rays. The resulting normalized theoretical retroreflected power from this structure is shown in the surface distribution of Fig. 2(a) as a function of the azimuthal angle ϕ and polar angle θ. As expected, the retroreflected power is diminished for orientations with glancing incidence upon any of the PC sensor electrodes, and the retroreflected power is maximized when $\phi = 45^\circ$ and $\theta = \cos(1/\sqrt{3}) \approx 54.7^\circ$. Thus, for optimal operation in a bidirectional optical link, the PC sensor should be aligned along this central and balanced orientation, with the incident light beams from the remote transmitter/source node of interest entering along the $(-n_1, -n_2, -n_3) = (-1/\sqrt{3}, -1/\sqrt{3}, -1/\sqrt{3})$ direction. The multitone frequency-biasing, sensing, and triangulation in the following subsection will provide a control mechanism to achieve this balanced and optimized-link condition.

3.2. Requirement II: Active (Unidirectional) Optical Downlink Detection

The second requirement for the success of FSO active downlink operation relates to unidirectional transmission from the transmitter/source node to the receiving node. The detection of such signals is often accomplished at the receiving node by way of a simple photodiode. The present investigation differs from this approach. The optical sensing mechanism in the proposed retroreflection/detection architecture provides a tool for sensing, alignment, and real-time control via multichannel balancing. Bringing the system into the balanced position optimizes the unit for both maximal retroreflection in passive uplink operation (as shown in the previous subsection) and maximal local signal reception in active downlink operation (as shown in this subsection).

PC switches are the primary choice for the incorporated design, as such structures provide nonrectified current–voltage responses (in contrast to the asymmetric diode responses of photodiodes). The linear response of PC switches allows the three AC bias signals at frequencies f_1, f_2, and f_3 to appear undistorted and DC background free on the output vertex electrode with their peak photocurrent amplitudes weighted proportionally by the incident PC_1, PC_2, and PC_3 optical powers.

Given a uniform intensity over the entire structure, the capture cross section of incident photons for each PC gap will change as the device is rotated. The photoconduction length l and width w across the PC gaps, being structural quantities, remain constant, while the optical intensity on each gap varies with the azimuthal ϕ and polar θ rotational angles of the device. This rotational dependence is visually apparent from the coordinate axes of Fig. 1(b). Given, for example, incident light at a small polar angle ($\theta \approx 0^\circ$), one would expect a high level of photoconductivity in PC_3 and a strong photocurrent signal on the output vertex electrode at the bias frequency f_3. The photoconductivity and output signals of PC_1 and PC_2 would then be negligible. Likewise, an orientation with a small azimuthal angle $\phi \approx 0^\circ$ will lead to a large PC_2 photocurrent signal at the output, and an orientation with a large azimuthal angle $\phi \approx 90^\circ$ will lead to a large PC_1 photocurrent signal at the output.

To quantify the above arguments, an algebraic analysis for the angular photocurrent dependence is carried out. The extent of this theoretical analysis is complicated by the internal reflections within

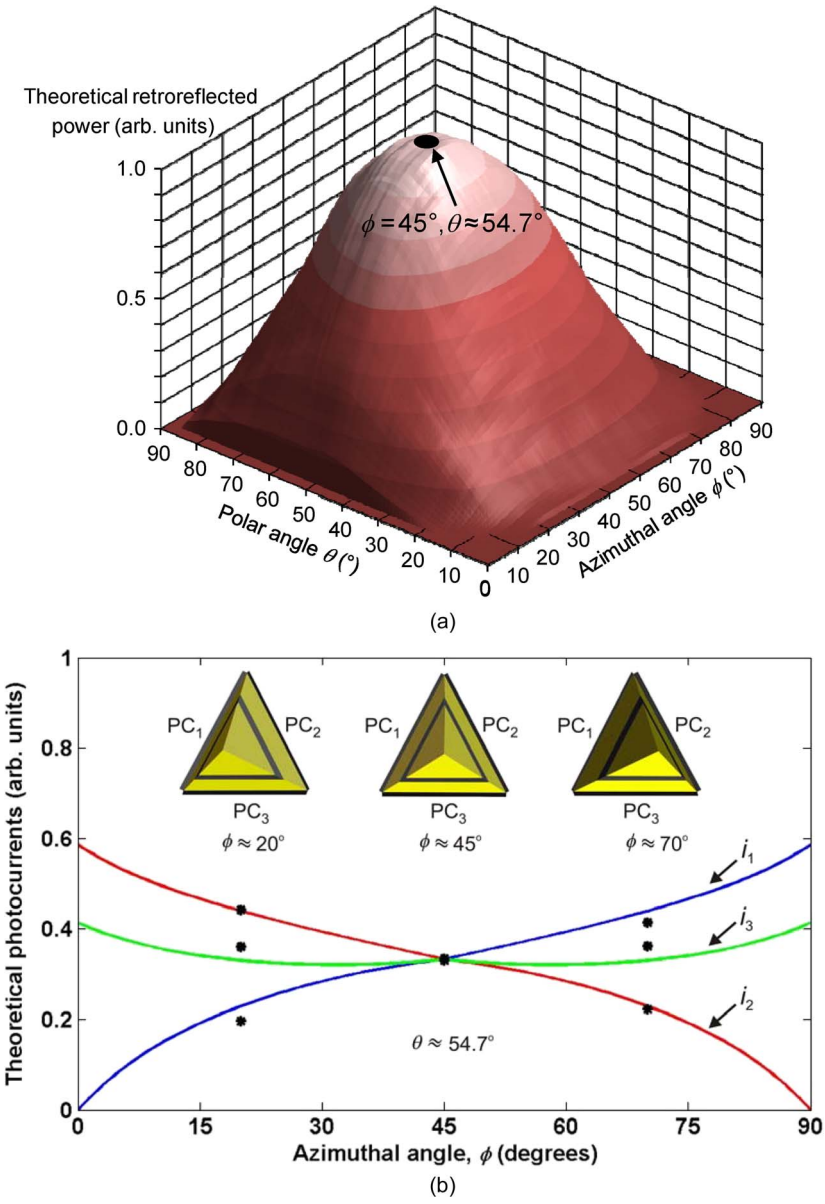

Fig. 2. Theoretical responses of the PC sensor are shown by way of the (a) retroreflected power and (b) photocurrent signals. The photocurrents i_1, i_2, and i_3 are shown as solid curves for a polar angle of $\theta \approx 54.7°$ and azimuthal angles in the range of $0° < \phi < 90°$. Experimental data points, given a 5-m optical link length, are also shown in the figure for a polar angle of $\theta \approx 54.7°$ and azimuthal angles of $\phi \approx 20°$, $\phi \approx 45°$, and $\phi \approx 70°$.

the corner cube. The incident light on any particular PC gap is comprised of illumination directly from the transmitter/source node, illumination that has reflected off of one neighboring electrode, and illumination as reflected off of two neighboring electrodes. Given the high reflectivity of Au, the photocurrent contributions from the reflected scenarios can be appreciable. Thus, these reflections are taken into account in the present theoretical model.

For brevity, the PC sensor operation is analyzed theoretically with a polar angle $\theta \approx 54.7°$ that is optimal for retroreflection and detection. The azimuthal angle ϕ is varied as the independent variable, while incident light rays with normalized directional cosine components $n_1 = \cos\phi\sin\theta$, $n_2 = \sin\phi\sin\theta$, and $n_3 = \cos\theta$ in the respective x-, y-, and z-directions and their resulting reflections,

TABLE 1

Theoretical normalized photocurrent expressions for the PC_1, PC_2, and PC_3 switches are tabulated for a polar angle of $\theta \approx 54.7^\circ$ and azimuthal angles in the range $0^\circ < \phi < 90^\circ$. The PC gap photocurrents gap are an additive result of direct illumination, one prior reflection from one neighbouring electrodes, and two prior reflections from neighbouring electrodes with an electrode reflectivity of $R = 97\%$. The illumination cases lead to the four displayed ray conditions on the incident light ray's normalized directional cosine components n_1, n_2, and n_3 in the *x*-, *y*-, and *z*-directions, respectively

Ray conditions	PC_1 photocurrent, i_1	PC_2 photocurrent, i_2	PC_3 photocurrent, i_3
1. $n_1 \le n_3 \le n_2$ $2n_3 \le (n_1 + n_2)$	$n_1 + Rn_1 + R\frac{n_1 n_3}{n_1 + n_2 - n_3} + R^2\frac{3n_1 n_3}{n_1 + n_2 + n_3}$	$n_2 + R\frac{n_1 n_2}{n_2 + n_3 - n_1} + R\frac{n_2 n_3}{n_1 + n_2 - n_3} + R^2 n_2\left(\frac{2n_1 - n_2 + 2n_3}{n_1 + n_2 + n_3}\right)$	$n_3 + Rn_3 + R\frac{n_1 n_3}{n_2 + n_3 - n_1} + R^2\frac{3n_1 n_3}{n_1 + n_2 + n_3}$
2. $n_1 \le n_3 \le n_2$ $2n_3 > (n_1 + n_2)$	$n_1 + 2Rn_1 + R^2 n_1$	$n_2 + Rn_2 + R\frac{n_2 n_1}{n_2 + n_3 - n_1} + R^2\frac{3n_1 n_2}{n_1 + n_2 + n_3}$	$n_3 + Rn_3 + R\frac{n_1 n_3}{n_2 + n_3 - n_1} + R^2\frac{3n_1 n_3}{n_1 + n_2 + n_3}$
3. $n_2 < n_3 < n_1$ $2n_3 \le (n_1 + n_2)$	$n_1 + R\frac{n_1 n_2}{n_1 + n_3 - n_2} + R\frac{n_1 n_3}{n_1 + n_2 - n_3} + R^2 n_1\left(\frac{2n_2 - n_1 + 2n_3}{n_1 + n_2 + n_3}\right)$	$n_2 + Rn_2 + R\frac{n_2 n_3}{n_1 + n_2 - n_3} + R^2\frac{3n_2 n_3}{n_1 + n_2 + n_3}$	$n_3 + Rn_3 + R\frac{n_2 n_3}{n_1 + n_3 - n_2} + R^2\frac{3n_2 n_3}{n_1 + n_2 + n_3}$
4. $n_2 < n_3 < n_1$ $2n_3 > (n_1 + n_2)$	$n_1 + Rn_1 + R\frac{n_1 n_2}{n_1 + n_3 - n_2} + R^2\frac{3n_1 n_2}{n_1 + n_2 + n_3}$	$n_2 + 2Rn_2 + R^2 n_2$	$n_3 + Rn_3 + R\frac{n_2 n_3}{n_1 + n_3 - n_2} + R^2\frac{3n_2 n_3}{n_1 + n_2 + n_3}$

are projected in the device. The resulting cases and subcases from the numerous reflections are then summed for the PC_1, PC_2, and PC_3 gaps. The resulting photocurrent expressions for i_1, i_2, and i_3 are summarized in Table 1. Note that the polar angle constraint of $\theta \approx 54.7^\circ$ restricts the normalized directional cosine components to two direct-ray conditions, i.e., $n_1 \le n_3 \le n_2$ and $n_2 \le n_3 \le n_1$, and two reflected-ray conditions, i.e., $2n_3 \le (n_1 + n_2)$ and $2n_3 > (n_1 + n_2)$.

The theoretical curves for the photocurrent expressions are shown in Fig. 2(b) for the fixed polar angle $\theta \approx 54.7^\circ$ and azimuthal angles ϕ ranging from 0° to 90°. The ability for angular-dependent mapping of the structure's orientation onto the PC_1, PC_2, and PC_3 photocurrents is immediately apparent in the figure. Given light incident along the *x*-axis with $\phi \approx 0^\circ$, the photocurrent i_1 is negligible, the photocurrent i_2 is maximal, and the photocurrent i_3 is at an intermediate level. Likewise, given light incident along the *y*-axis with $\phi \approx 90^\circ$, the photocurrent i_1 is maximal, the photocurrent i_2 is negligible, and the photocurrent i_3 is at an intermediate level. Between these extremes exists the desired balanced condition with $\phi = 45^\circ$, where all of the photocurrents are equal. The alignment of the system to this balanced state is accomplished in the frequency domain with the multitone frequency-biasing arrangement introduced in the following experimental section.

4. Experimental Analysis

To test the retroreflection and detection capabilities of the proposed PC sensor, the device is fabricated as described in Section 2, and its operation is analyzed in a 5-m indoor controlled bidirectional FSO enclosure environment. A 100-mW, 785-nm laser diode is employed as a point-to-point test source, as such a source provides above-bandgap semiconductor photon absorption with the incorporated 1.43 eV semi-insulating GaAs bandgap. The point-to-point laser configuration is chosen here to characterize the PC sensor reflection/detection responses that are due solely to the physical device, as multipath responses from the external environment are eliminated in such systems. Approximately 10 mW of optical power is retroreflected back to the laser from the uniformly illuminated and LC-modulated PC sensor. The PC sensor is activated with AC voltage waveforms on the PC_1, PC_2, and PC_3 bias electrodes using the configuration shown in Fig. 1(b). The bias signal for PC_1 is $v_{bias,f1}$ at a frequency of $f_1 = 1.5$ kHz, the bias signal for PC_2 is $v_{bias,f2}$ at a frequency of $f_2 = 3.3$ kHz, and the bias signal for PC_3 is $v_{bias,f3}$ at a frequency of $f_3 = 2.4$ kHz. The biasing frequencies are selected to avoid aliasing between the f_1, f_2, and f_3 fundamental signals and all signal harmonics. The resulting individual PC photocurrents are then summed at the vertex electrode to produce a total photocurrent output i_{total}. This total photocurrent is ultimately processed by the electronic amplifier and broadband/narrowband filters shown in Fig. 1(c). The bandwidth of the narrowband filters is chosen to pass the signal of interest while blocking the neighboring signals. At the same time, this narrowband filtering minimizes extraneous optical noise and background light levels within the environment.

To test the detection capabilities of the PC sensor, the device is uniformly illuminated by the optical source, and the PC sensor photocurrents are monitored while the device is rotated in a gyroscope. Independent rotations of ϕ and θ are used, and the results are displayed in the frequency domain in Fig. 3. Fig. 3(a) shows results for an off-axis optical alignment with incident light entering at $\phi \approx 20^\circ$ and $\theta \approx 54.7^\circ$. The PC sensor, as viewed by the source, is shown in the inset. The imbalance in the optical alignment (with PC_2 having the greatest illumination and PC_1 having the lowest illumination) is immediately apparent in the results. The PC_2 photocurrent is the largest peak, followed by the PC_3 and PC_1 photocurrents, which reach 82% and 44% of the PC_2 maximum. These experimental data points are plotted with the theoretical curves of Fig. 2(b) and are seen to be in good agreement (3% error). Fig. 3(b) shows the results of off-axis optical alignment with $\phi \approx 70^\circ$ and $\theta \approx 54.7^\circ$. In this new case, PC_1 has the greatest illumination and PC_2 the lowest. The imbalance is apparent in the frequency domain, as the PC_3 and PC_2 photocurrents reach 88% and 54% of the PC_1 maximum. The measured photocurrents are plotted with the theoretical curves of Fig. 2(b) and are again seen to be in good agreement (3% error).

The alignment-balancing procedure for the device is performed by noting disparities in the photocurrent frequency peaks and rotating the structure to eliminate these disparities. This process is carried out with the PC sensor mounted in a gyroscope. Rotations are used to balance the peak frequency amplitudes, and the structure is ultimately left in the alignment orientation in which $\theta \approx 54.7^\circ$ and $\phi \approx 45^\circ$. The frequency-domain signal for this orientation is shown in Fig. 3(c). In this orientation the structure (shown as viewed by the source in the inset) is balanced, and the photocurrents produced by PC_1, PC_2, and PC_3 are approximately equal (within 0.2% error). Such an orientation corresponds to an optical alignment with the incident light rays entering the device along the $(-n_1, -n_2, -n_3) = (-1/\sqrt{3}, -1/\sqrt{3}, -1/\sqrt{3})$ direction. This orientation is optimized for both maximal retroreflection in passive bidirectional uplink operation (as shown in Section 3) and maximal signal reception in active unidirectional downlink detection (as it can be shown that i_{total} reaches a maximum in this balanced orientation).

Given the above alignment and balancing procedure, the structure is left in an orientation that is optimized for passive optical communication by way of optical modulation. This proof-of-principal scenario is tested here with a Pi-cell LC optical modulator mounted over the entrance interface of the device. During illumination of the device, the attenuation of the LC window is modulated at a 100-Hz frequency, while the signal returning to the optical transmitter/source is monitored. These

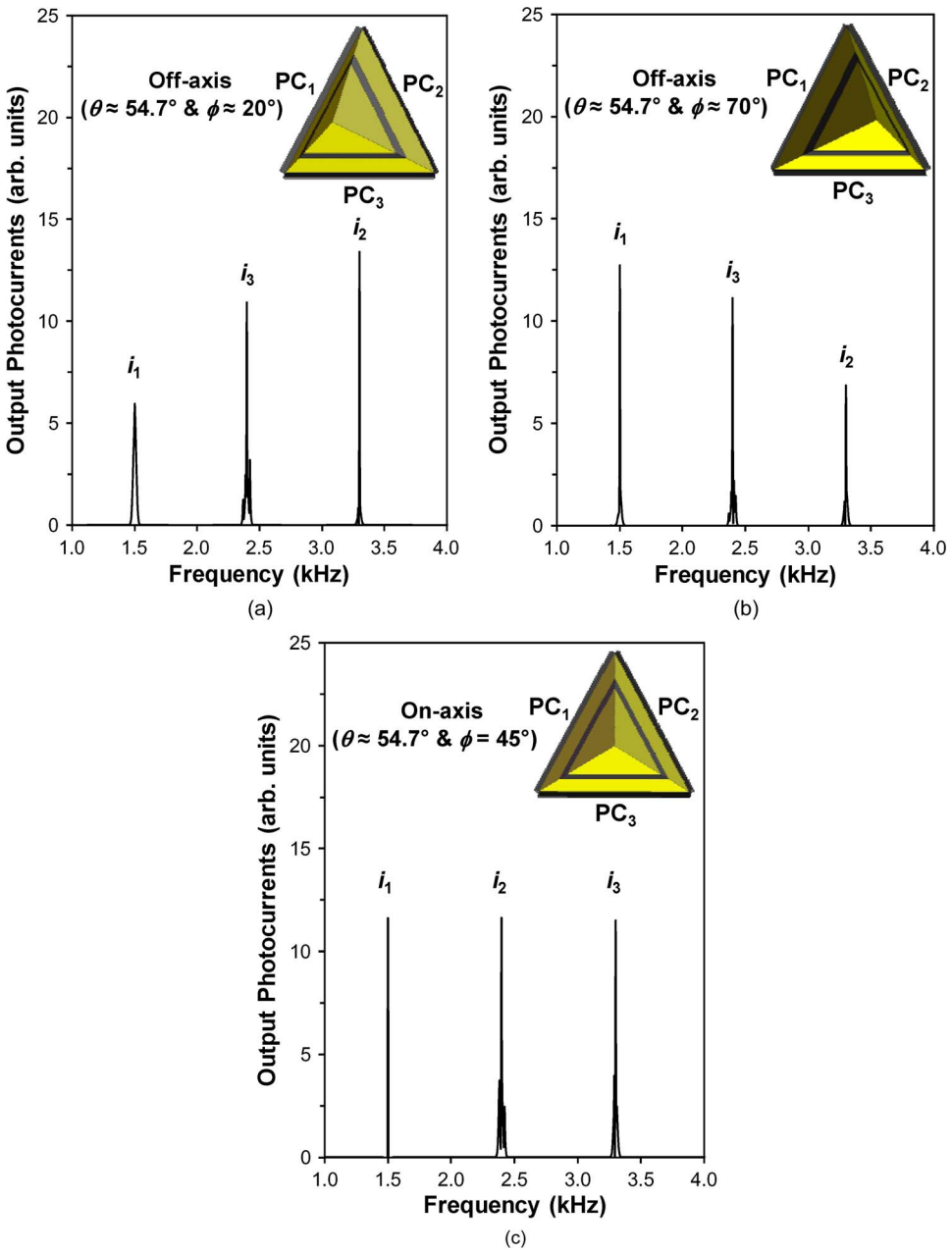

Fig. 3. Experimental frequency-domain photocurrents for the recorded GaAs PC output signals are shown for PC_1, PC_2, and PC_3, respectively. The misalignment (off-axis) results are shown for (a) $\phi \approx 20^\circ$, $\theta \approx 54.7^\circ$ and (b) $\phi \approx 70^\circ$, $\theta \approx 54.7^\circ$ with the differing signal strengths, while the optimal alignment (on-axis) results are shown for (c) $\phi = 45^\circ$, $\theta \approx 54.7^\circ$ with the balanced/equal signal strengths. The figure inset shows the PC sensor as viewed from the source at the respective orientations.

retroreflected power results are shown in Fig. 4(a) and (b) for the time and frequency domains, respectively. The LC modulation applied on the PC sensor and measured at the optical transmitter/source node is particularly evident from these signals, as the 100-Hz modulation frequency is observed with a signal-to-noise ratio (SNR) beyond 30 dB. The strength of the signal seen here is attributed to the narrowband filtering of extraneous noise sources in the environment and the enhanced signal power from the employed PC sensor alignment-balancing procedure.

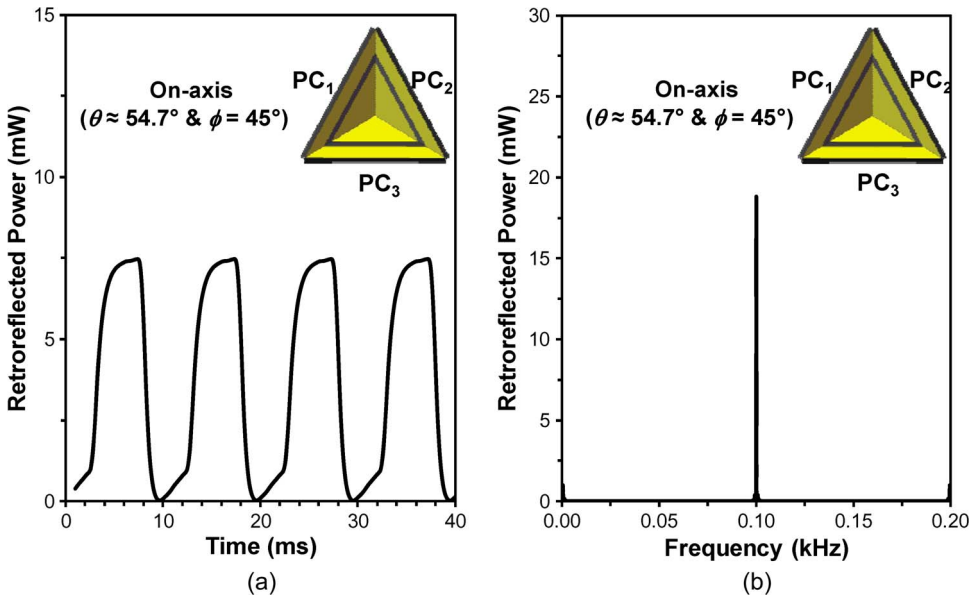

Fig. 4. Experimental (a) time-domain and (b) frequency-domain waveforms for the retroreflected optical power level returned to the transmitter/source node are shown for continuous laser illumination with a Pi-cell LC modulator on the PC sensor. The results are shown for the optimal (on-axis) alignment with $\phi = 45^\circ$ and $\theta \approx 54.7^\circ$ given a 5-m optical link length. The figure inset shows the PC sensor orientation as viewed from the source.

5. Conclusion

In this paper, a multitone biasing arrangement was demonstrated with a three-electrode PC sensor architecture. The device was shown to be well suited for FSO applications, as it can successfully establish bidirectional passive uplinks between the PC sensor and remote transmitter/source node(s) and provide unidirectional reception of incident optical signals from the remote transmitter/source node(s). Furthermore, the threefold symmetry of the PC sensor structure and multitone biasing together were shown to offer a frequency-domain balancing mechanism that optimizes the alignment for retroreflection and detection. The device was analyzed theoretically and experimentally, and proof-of-principal FSO communication was demonstrated over an indoor 5-m link length. Such structures will be well suited to future FSO communication networks incorporating isolated (small scale) optical transceiver nodes as well as arrayed (large-scale) implementations incorporating interleaved multicorner-cube retrosurfaces.

References

[1] W.-K. Huang, Y.-C. Liu, and Y.-M. Hsin, "A high-speed and high-responsivity photodiode in standard CMOS technology," *IEEE Photon. Technol. Lett.*, vol. 19, no. 4, pp. 197–199, Feb. 2007.
[2] J. F. Holzman, F. E. Vermeulen, and A. Y. Elezzabi, "Generation of 1.2 ps electrical pulses through parallel-gating in ultra-thin silicon photoconductive switches," *Appl. Phys. Lett.*, vol. 79, no. 25, pp. 4249–4251, Dec. 2001.
[3] G. D. Pitt, P. Extance, R. C. Neat, D. N. Batchelder, R. E. Jones, J. A. Barnett, and R. H. Pratt, "Optical-fibre sensors," *Proc. Inst. Elect. Eng. J. Optoelectron.*, vol. 132, no. 4, pp. 214–248, Aug. 1985.
[4] D. Kedar and S. Arnon, "Urban optical wireless communication networks: The main challenges and possible solutions," *IEEE Commun. Mag.*, vol. 42, no. 5, pp. S2–S7, May 2004.
[5] X. Zhu and J. M. Kahn, "Free-space optical communication through atmospheric turbulence channels," *IEEE Trans. Commun.*, vol. 50, no. 8, pp. 1293–1300, Aug. 2002.
[6] S. Junique, D. Agren, Q. Wang, S. Almqvist, B. Noharet, and J. Y. Andersson, "A modulating retro-reflector for free-space optical communication," *IEEE Photon. Technol. Lett.*, vol. 18, no. 1, pp. 85–87, Jan. 2006.
[7] W. Mao and J. M. Kahn, "Free-space heterochronous imaging reception of multiple optical signals," *IEEE Trans. Commun.*, vol. 52, no. 2, pp. 269–279, Feb. 2004.
[8] T. Tsujimura, T. Yano, and K. Yoshida, "Transmission laser beam control method for ubiquitous free space optics," in *Proc. IEEE SICE Conf.*, 2004, vol. 1, pp. 599–604.

[9] N. Ahmed, M. I. Anis, and Farhan, "System level designing of FSO link through LED and NRZ modulation scheme by using different filters," in *Proc. IEEE MMS Conf.*, 2009, pp. 1–4.
[10] X. Jin, J. E. Barg, and J. F. Holzman, "Retro-detective control structures for free-space optical communication links," *Opt. Express*, vol. 17, no. 26, pp. 23 867–23 872, Dec. 2009.
[11] S. Winnerl, F. Peter, S. Nitsche, A. Dreyhaupt, B. Zimmermann, M. Wagner, H. Schneider, M. Helm, and K. Kohler, "Generation and detection of THz radiation with scalable antennas based on GaAs substrates with different carrier lifetimes," *IEEE J. Sel. Areas Commun.*, vol. 14, no. 2, pp. 449–457, Mar./Apr. 2008.
[12] C. Jenkins, W. Johnstone, D. Uttamchandani, V. Handerek, and S. Radcliffe, "MEMS actuated spherical retroreflector for free-space optical communications," *Electron. Lett.*, vol. 41, no. 23, pp. 1278–1279, Nov. 2005.
[13] L. Zhou, J. M. Kahn, and K. S. J. Pister, "Corner-cube retroreflectors based on structure-assisted assembly for free-space optical communication," *J. Microelectromech. Syst.*, vol. 12, no. 3, pp. 233–242, Jun. 2003.
[14] D. C. O'Brien, W. W. Yuan, J. J. Liu, G. E. Faulkner, S. J. Elston, S. Collins, and L. A. Parry-Jones, "Optical wireless communications for micro-machines," in *Proc. SPIE*, 2006, vol. 6304, pp. 630 4A1–630 4A8.
[15] S. Arnon, "Network of sensors: Acquisition probability," *J. Opt. Soc. Amer. A, Opt. Image Sci.*, vol. 24, no. 9, pp. 2758–2765, Sep. 2007.
[16] L. Sjöqvist, E. Hällstig, J. Öhgren, L. Allard, D. Ågren, S. Junique, Q. Wang, B. Noharet, D. Engström, and S. Hård, "A novel free-space retrocommunication link," *Proc. SPIE*, vol. 5614, pp. 10–23, 2004.
[17] G. C. Gilbreath, W. S. Rabinovich, T. J. Meehan, M. J. Vilcheck, R. Mahon, R. Burris, M. Ferraro, I. Solkolsky, J. A. Vasquez, C. S. Bovais, K. Cochrell, K. C. Goins, R. Barbehenn, D. S. Katzer, K. Ikossi-Anastasiou, and M. J. Montes, "Large-aperture multiple quantum well modulating retroreflector for free-space optical data transfer on unmanned aerial vehicles," *Opt. Eng.*, vol. 40, no. 7, pp. 1348–1356, Jul. 2001.
[18] J. M. Kahn, R. H. Katz, and K. S. J. Pister, "Emerging challenges: Mobile networking for 'smart dust'," *J. Commun. Netw.*, vol. 2, no. 3, pp. 188–196, Sep. 2000.
[19] B. Warneke, M. Last, B. Liebowitz, and K. S. J. Pister, "Smart dust: Communicating with a cubic-millimeter computer," *Computer*, vol. 34, no. 1, pp. 44–51, Jan. 2001.
[20] C. M. Collier, X. Jin, J. F. Holzman, and J. Cheng, "Omni-directional characteristics of composite retroreflectors," *J. Opt. A., Pure Appl. Opt.*, vol. 11, no. 8, pp. 085 404-1–085 404-10, Aug. 2009.